

# M2MRF: Many-to-Many Reassembly of Features for Tiny Lesion Segmentation in Fundus Images

Qing Liu, Haotian Liu, Yixiong Liang<sup>1</sup>

<sup>1</sup>School of Computer Science, Central South University

## Abstract

Feature reassembly is an essential component in modern CNNs-based segmentation approaches, which includes feature downsampling and upsampling operators. Existing feature reassembly operators reassemble multiple features from a small predefined region into one for each target location independently. This may result in loss of spatial information, which could vanish activations of tiny lesions particularly when they cluster together. In this paper, we propose a many-to-many reassembly of features (M2MRF). It reassembles features in a dimension-reduced feature space and simultaneously aggregates multiple features inside a large predefined region into multiple target features. In this way, long range spatial dependencies are captured to maintain activations on tiny lesions, particularly when multiple lesions coexist. Experimental results on two lesion segmentation benchmarks, i.e. DDR and IDRiD, show that our M2MRF outperforms existing feature reassembly operators.

## 1. Introduction

This paper focuses on segmentation of tiny lesions, e.g. soft exudates (SEs), hard exudates (EXs), microaneurysms (MAs) and hemorrhages (HEs) (see Fig. 1) in colour fundus images, which is an important prerequisite for enabling computers to assist human doctors for clinical purpose. It falls into the research area of semantic segmentation.

With the rise of deep convolutional neural networks (CNN), many CNNs-based approaches such as (Long, Shelhamer, and Darrell 2015; Ronneberger, Fischer, and Brox 2015; Xie and Tu 2015; Chen et al. 2017; Zhao et al. 2017; Chen et al. 2018; Wang et al. 2020) have been proposed for semantic segmentation and achieved extraordinary progress. On Cityscape (Cordts et al. 2016) with 19 classes, the mean of class-wise intersection over union (mIoU) by the state-of-the-art approach HRNetV2 (Wang et al. 2020) has been improved to 81%. However, when fine-tuning HRNetV2 (Wang et al. 2020) for four-class lesion segmentation in fundus images, the mIoU on IDRiD (Porwal et al. 2020) decreases to 47%. Why is lesion segmentation so much harder than natural scene image segmentation? Two possible factors behind performance gap are the extreme small size of lesions and large scale variation across them. Interestingly, almost 50% lesions are less than 256 pixels in images of size  $4288 \times 2848$  from IDRiD (Porwal et al. 2020) dataset

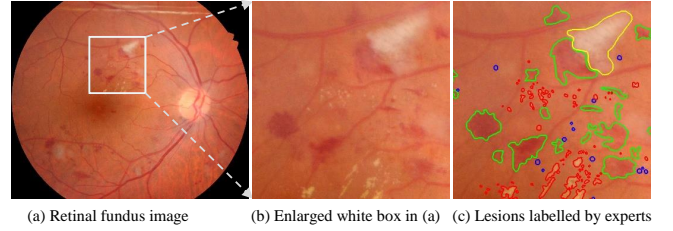


Figure 1: Example for colour fundus images and lesions. Four types of lesions i.e. SEs, EXs, MAs and HEs are delineated in yellow, red, blue and green respectively. Many lesions are extremely small and the size variance across them are enormous.

provided by the 2018 ISBI grand challenge. Such tiny size of lesions presents an extreme challenge for CNN-based segmentation approaches to learn discriminative representations with enough spatial information. To make matters worse, the smallest 10% lesions in IDRiD (Porwal et al. 2020) only contain less than 74 pixels while the largest 10% lesions contain more than 1920 pixels. Such enormous size variation rises a new challenge for CNN-based approaches to learn representations with adaptive receptive field. Moreover, in fundus images, multiple lesions with large size variation always coexist and cluster together, which makes the representation learning more challenge.

Taking an in-depth look at modern CNN-based segmentation approaches (Long, Shelhamer, and Darrell 2015; Ronneberger, Fischer, and Brox 2015; Xie and Tu 2015; Chen et al. 2017; Zhao et al. 2017; Chen et al. 2018; Sun et al. 2019; Wang et al. 2020), the challenges of applying them to lesion segmentation are mainly caused by the repetitive utilisation of operators for reassembly of features (RF operators for short), i.e. downsampling and upsampling operators. Strided max-pooling and strided convolution (Springenberg et al. 2015; Sun et al. 2019; Wang et al. 2020) are two widely-adopted operators for downsampling, while bilinear interpolation and deconvolution are two common choices for upsampling. These four RF operators assume that features in target feature map are independent and follow a many-to-one pipeline. They first determine a small local region in input feature map, according to a target location in output

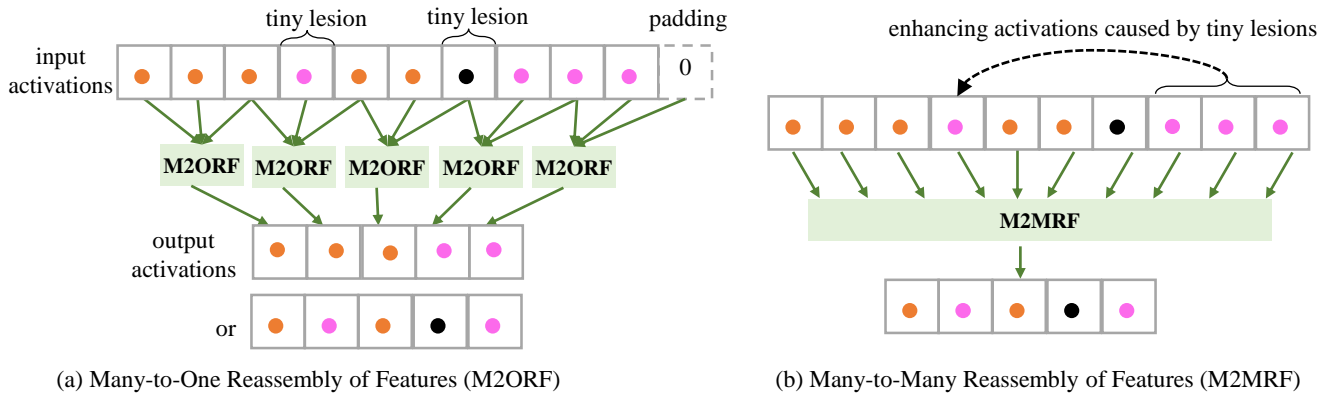


Figure 2: Illustration of our motivation. Solid circles in black, orange and magenta indicate activations mainly caused by three different classes. Here we take the downsampling with rate of 2 for example. With the input activations, we want to preserve activations of both large lesions and tiny lesions. M2ORF reassembles multiple features inside a small local region and outputs one activation, as illustrated in (a). It ignores the coexist of multiple lesions, which may result in dilution or even vanishing of activations of tiny lesions. Feature reassembly operators should consider the coexist of multiple lesions and learn to reassemble activations inside a large local region to generate multiple output activations simultaneously, as illustrated in (b).

feature map. Then they reassemble multiple features in the small local region into one as the output feature for the target location. However, the many-to-one reassembly of features (M2ORF) operators often ignore the coexist of multiple lesions and fail to utilise the long-range dependencies to enhance activations caused by tiny lesions. These further lead to dilution or even vanishing of activations of tiny lesions, as illustrated in Fig. 2(a).

In this paper, we aim to address these issues raised by M2ORF operators within the context of tiny lesion segmentation. Basically, we pursue a RF operator that is capable of 1) preserving activations caused by tiny lesions particularly when they coexist with large lesions; 2) easily being integrated into existing CNN-based segmentation models. To this end, we propose a lightweight RF operator, termed as Many-to-Many Reassembly of Features (M2MRF), which considers the coexist of lesions in variant sizes and reassembles multiple features inside a large predefined region into multiple target features simultaneously (see Fig.2(b)).

We demonstrate the effectiveness of our M2MRF on two public tiny lesion segmentation datasets, i.e. DDR (Li et al. 2019) and IDRiD (Porwal et al. 2020). Experiments show that our M2MRF outperforms state-of-the-art RF operators. Particularly, compared with a strong segmentation baseline HRNetv2 (Wang et al. 2020), our M2MRF exhibits significant improvements with negligible increase of parameters and inference time.

## 2. Related Work

**Feature Reassembly Operators in Deep Networks.** In existing deep networks (Long, Shelhamer, and Darrell 2015; Ronneberger, Fischer, and Brox 2015; Noh, Hong, and Han 2015; Badrinarayanan, Kendall, and Cipolla 2017; Chen et al. 2017, 2018; Sun et al. 2019; Wang et al. 2020), strided max-pooling (LeCun et al. 1990) and strided convolution are two widely-adopted operators for feature down-

sampling. Bilinear interpolation, deconvolution and unpooling (Zeiler, Taylor, and Fergus 2011; Zeiler and Fergus 2014) are widely-adopted for feature upsampling. The general idea of these operators is to generate a feature vector for each target location via reassembling multiple features inside a predefined region with importance kernels. Particularly, importance kernels for strided max-pooling, unpooling and bilinear interpolation are hand-crafted and feature maps are processed channel-by-channel efficiently. However, they ignore the context dependencies across channels and the diversity of local patterns. Instead, the importance kernels for strided convolution and deconvolution are learned. Their dimension depends on the input feature dimension, which is always high in CNNs. This makes the computation burden of reassembly heavy when large importance kernels are used. Thus it is difficult to reassemble features from a large region.

Recently, novel ideas about learning-based RF operators emerge. LIP (Gao, Wang, and Wu 2019) learns adaptive importance kernels based on inputs to enhance the discriminative features. In CARAFE (Wang et al. 2019) and CARAFE++ (Wang et al. 2021), content-aware kernels for each target position is learned according to input features for feature reassembly. Similarly, IndexNet (Lu et al. 2019, 2020) learns importance kernels from feature encoder to guide the feature reassembly in both feature encoder and decoder. Instead of reassembling features inside a predefined region, deformable RoI pooling (Dai et al. 2017) reassembles features in an adaptive region which is learned from the input features. To model the affinity information,  $A^2U$  (Dai, Lu, and Shen 2021) is proposed to learn importance kernels according to second-order features for feature reassembly. However, these learning-based operators still follow the framework of many-to-one feature reassembly and are prone to dilute or even vanish features of tiny lesions.

**Tiny lesion segmentation in Fundus Images.** The development originated from one-type lesion segmentation with

either hand-crafted features (Zhang et al. 2014; Liu et al. 2017; Du et al. 2020) or deep features (Liu et al. 2021a) and has been evolved to multi-type lesion segmentation. For example, in work (Li et al. 2019), PSPNet (Zhao et al. 2017) and DeeplabV3+ (Chen et al. 2018) are directly fine-tuned for multi-type lesion segmentation. Guo et al. (Guo et al. 2019) built a network named L-Seg on FCN (Long, Shelhamer, and Darrell 2015). All of those methods adopt many-to-one RF operators during feature encoding and decoding and are prone to ignore tiny lesions. One thing worth to mention is that the public datasets with pixel-level annotations also updates from one-type lesion segmentation e.g. E-ophtha EX (Decenciere et al. 2013) and e-ophtha MA (Decenciere et al. 2013) to multi-type lesion segmentation e.g. IDRiD (Porwal et al. 2020) and DDR (Li et al. 2019).

**Deep Semantic segmentation.** The development can be mainly classified into three veins. The first vein focuses on how to produce and aggregate multi-scale representations. FCN (Long, Shelhamer, and Darrell 2015) provides a natural solution which reuses middle-level features to compensate for spatial details in high-level features. UNet (Ronneberger, Fischer, and Brox 2015) propagates low-level information to high-levels via skip connections. In (Li et al. 2020), gated fully fusion is proposed to selectively fuse multi-level features. The second vein focuses on high-resolution representation learning. For example, in (Ronneberger, Fischer, and Brox 2015; Noh, Hong, and Han 2015; Badrinarayanan, Kendall, and Cipolla 2017), an encoder-decoder architectural style is adopted to gradually recover feature resolution while HRNet (Sun et al. 2019; Wang et al. 2020) is specially designed to learn high-resolution representations. The third vein introduces attention mechanism and variant modules such as DANet (Fu et al. 2019), DRANet (Fu et al. 2020), CCNet (Huang et al. 2019), RecoNet (Chen et al. 2020), HANet (Choi, Kim, and Choo 2020) and DNL (Yin et al. 2020) are developed to explore long range dependencies. More recently, vision transformers such as Swin (Liu et al. 2021b), Twins (Chu et al. 2021) and CSWin (Dong et al. 2021) are developed for segmentation. However, those methods are designed for segmenting objects in proper size rather than tiny size.

### 3. Method

In this section, we first give a simple analysis for M2ORF operators and then detail our M2MRF. Finally we take HRNetV2 (Wang et al. 2020) as an example and present how to integrate our M2MRF into CNN-architectures for tiny lesion segmentation.

#### 3.1 Analysis for M2ORF Operators

Given the input feature map  $\mathbf{X} \in \mathcal{R}^{H \times W \times C}$  and sample rate  $\delta$  where  $\delta > 0$ , the goal of feature reassembly is to generate target feature map  $\mathbf{Y} \in \mathcal{R}^{[\delta H] \times [\delta W] \times C}$  via finding a function mapping  $\Phi$  parametrised by importance kernels  $\mathbf{W}$ :

$$\mathbf{Y} = \Phi(\mathbf{X}; \mathbf{W}). \quad (1)$$

Here  $\delta < 1$  for downsampling and  $\delta > 1$  for upsampling.

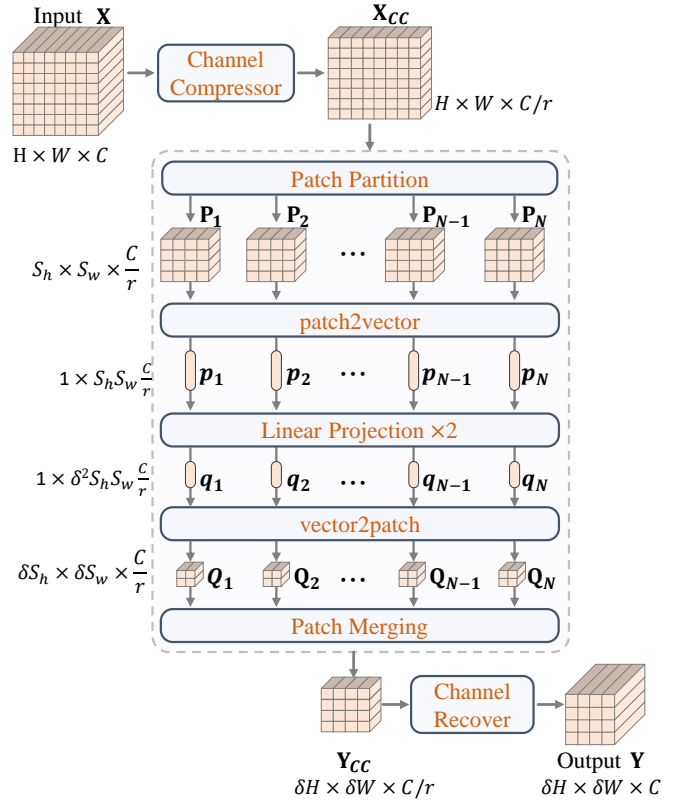


Figure 3: An overview of our Many-to-Many Reassembly of Features (M2MRF).  $\{\mathbf{P}_n\}_{n=1}^N$  and  $\{\mathbf{Q}_n\}_{n=1}^N$  are feature patches of size  $S_h \times S_w \times \frac{C}{r}$  and  $\delta S_h \times \delta S_w \times \frac{C}{r}$  respectively, where  $N(= \lceil H/S_h \rceil \cdot \lceil W/S_w \rceil)$  is the number of patches.  $\{\mathbf{p}_n\}_{n=1}^N$  and  $\{\mathbf{q}_n\}_{n=1}^N$  are feature vectors. In this figure, a feature map of size  $H \times W \times C$  is downsampled by a factor of  $\delta(= 1/2)$ . (Best view in color)

To make the feature reassembly computational efficient, most existing methods degrade it to a many-to-one local sampling problem, i.e. reassembling multiple features in a predefined local region to one target feature. Specifically, for any target feature  $\mathbf{y} \in \mathcal{R}^C$  at location  $(i', j')$  in  $\mathbf{Y}$ , most existing methods assume that there is a corresponding source feature  $\mathbf{x} \in \mathcal{R}^C$  at location  $(i, j)$  in  $\mathbf{X}$ , where  $i = \lfloor i'/\delta \rfloor$  and  $j = \lfloor j'/\delta \rfloor$ . They follow three steps to obtain  $\mathbf{y}$ : (1) setting/learning a local region  $\Omega_{\mathbf{x}}$  according to  $\mathbf{x} \in \mathcal{R}^C$ ; (2) with  $\Omega_{\mathbf{x}}$ , setting/learning corresponding importance kernels  $\mathbf{W}_{i', j'}$ ; (3) obtaining  $\mathbf{y}$  via

$$\mathbf{y} = \Phi(\mathbf{P}_{\Omega_{\mathbf{x}}}; \mathbf{W}_{i', j'}), \quad (2)$$

where  $\mathbf{P}_{\Omega_{\mathbf{x}}}$  denotes features in  $\Omega_{\mathbf{x}}$ .

Obviously, M2ORF operators assume that each target feature in  $\mathbf{Y}$  is independent and ignore the coexist of multiple lesions. Additionally, considering the computational efficiency, previous RF operators such as strided convolution, deconvolution, CARAFE++ (Wang et al. 2021) and A<sup>2</sup>U (Dai, Lu, and Shen 2021) usually consider a small size  $\Omega_{\mathbf{x}}$ , which makes them fail to utilise long-range dependencies.

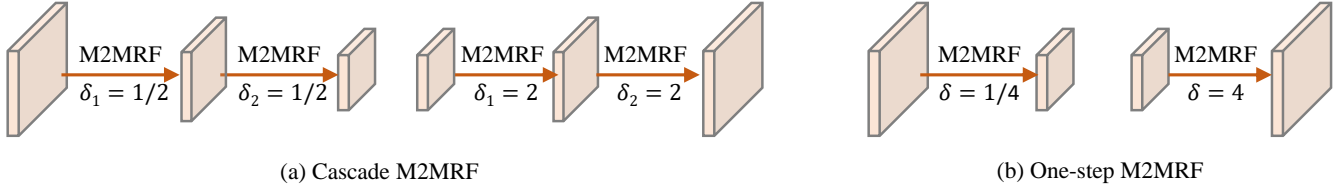


Figure 4: Two variants of our M2MRF. Here we take  $\delta = 4$  for upsampling and  $\delta = 1/4$  for downsampling as examples.

As a result, activations caused by tiny lesions are prone to be diluted or even vanished. To alleviate the dilution of tiny lesion activations, one natural solution is to discard the assumption of M2ORF and generate multiple features for multiple target locations with features inside a large local region simultaneously. To this end, we propose many-to-many reassembly of features (M2MRF).

### 3.2 Many-to-Many Reassembly of Features

**Overview.** Fig. 3 illustrates an overview of reassembling the input feature map  $\mathbf{X}$  of size  $H \times W \times C$  with our M2MRF operator with sample rate  $\delta$  to feature map  $\mathbf{Y}$  of size  $\delta H \times \delta W \times C$ . First, a channel compressor is performed on  $\mathbf{X}$  to reduce its channel from  $C$  to  $C/r$  for computational efficiency. We denote the output as  $\mathbf{X}_{CC}$ . Then we partition  $\mathbf{X}_{CC}$  into feature patches  $\{\mathbf{P}_n\}_{n=1}^N$  of size  $S_h \times S_w \times \frac{C}{r}$ , where  $N = \lceil H/S_h \rceil \cdot \lceil W/S_w \rceil$ . Our proposed M2MRF is performed on each feature patches and outputs  $\{\mathbf{Q}_n\}_{n=1}^N$  of size  $\delta H \times \delta W \times \frac{C}{r}$ . Thereafter, those patches are merged into feature map  $\mathbf{Y}_{CC}$  of size  $\delta H \times \delta W \times \frac{C}{r}$ . Finally, we recover the feature channel to  $C$  via channel recover. For channel compressor and recover, we simply implement them with a  $1 \times 1$  regular convolution layer.

**M2MRF.** With a local feature patch  $\mathbf{P} \in \{\mathbf{P}_n\}_{n=1}^N$ , the goal is to generate  $\mathbf{Q}$  of size  $\delta S_h \times \delta S_w \times \frac{C}{r}$ :

$$\mathbf{Q} = \Phi(\mathbf{P}; \mathbf{W}_{patch}). \quad (3)$$

Here we treat this task as generating  $\delta S_h \times \delta S_w$  features  $\mathbf{Q} = \{\mathbf{y}_m\}_{m=1}^{\delta^2 S_h S_w}$  from  $S_h \times S_w$  source features  $\mathbf{P} = \{\mathbf{x}_n\}_{n=1}^{S_h S_w}$  where  $\mathbf{y}_m, \mathbf{x}_n \in \mathcal{R}^{1 \times \frac{C}{r}}$ . To achieve this, one option is to adopt linear projection, thus Eqn.(3) can be expressed as:

$$[\mathbf{y}_1, \dots, \mathbf{y}_{\delta^2 S_h S_w}] = [\mathbf{x}_1, \dots, \mathbf{x}_{S_h S_w}] [\mathbf{W}_1, \dots, \mathbf{W}_{\delta^2 S_h S_w}], \quad (4)$$

where  $\mathbf{W}_1, \dots, \mathbf{W}_{\delta^2 S_h S_w}$  are parameters of size  $(S_h S_w \frac{C}{r}) \times \frac{C}{r}$  to be learned. Therefore we have  $\mathbf{W}_{patch} = [\mathbf{W}_1, \dots, \mathbf{W}_{\delta^2 S_h S_w}]$  whose size is  $(S_h S_w \frac{C}{r}) \times (\delta^2 S_h S_w \frac{C}{r})$ . For simplicity, we denote  $\mathbf{p} = [\mathbf{x}_1, \dots, \mathbf{x}_{S_h S_w}]$ ,  $\mathbf{q} = [\mathbf{y}_1, \dots, \mathbf{y}_{\delta^2 S_h S_w}]$ , and rewrite Eqn.(4) as:

$$\mathbf{q} = \mathbf{p} \mathbf{W}_{patch}. \quad (5)$$

As  $S_h S_w$  is required to be large to make use of long-range dependencies,  $\mathbf{W}_{patch}$  is always a large matrix. On one hand, it is always difficult to optimise such a large matrix. On the other hand, storing a large matrix results in high memory consumption. To reduce the number of parameters

to be learned, we decompose  $\mathbf{W}_{patch}$  to two small matrices via a two-layer linear projections. Thus Eqn. (4) can be rewrote as:

$$\mathbf{q} = (\mathbf{p} \mathbf{W}'_{patch}) \mathbf{W}''_{patch}, \quad (6)$$

where  $\mathbf{W}'_p \in \mathcal{R}^{(S_h S_w \frac{C}{r}) \times (S_h S_w \frac{C}{\alpha r})}$  and  $\mathbf{W}''_p \in \mathcal{R}^{(S_h S_w \frac{C}{\alpha r}) \times (\delta^2 S_h S_w \frac{C}{r})}$  are parameters in the two linear projections, and  $\alpha \geq 1$  such that the matrix dimension of  $\mathbf{W}'_{patch}$  and  $\mathbf{W}''_{patch}$  is less than  $\mathbf{W}_{patch}$  far away.

### 3.3 M2MRF for Tiny Lesion Segmentation

As HRNetV2 (Wang et al. 2020) is originally designed for high-resolution representation learning and has achieved state-of-the-art performance on semantic segmentation task, we adopt it as the baseline for tiny lesion segmentation. In HRNetV2 (Wang et al. 2020), RF operators involve in the fusion module to exchange information across multi-resolution feature maps. Strided convolution with stride of 2 is adopted for downsampling and bilinear interpolation for upsampling. Repeating  $t$  times of the strided convolution, the feature resolution decreases to  $1/2^t$ . To build M2MRF variants, we replace the repeated strided convolution and bilinear interpolation with our M2MRF.

We propose two options to replace the repeated  $t$  layers of strided convolution with our M2MRF. One is to replace each strided convolution layer with our proposed M2MRF with  $\delta = 1/2$  to gradually decrease the feature resolution. We term it as cascade M2MRF. The other is to directly set  $\delta$  to  $1/2^t$  in M2MRF to replace the  $t$  layers of strided convolution. We term it as one-step M2MRF. Similarly, there are also two options to replace bilinear interpolation layer with scale factor  $2^t$ . One is to cascade M2MRF with  $\delta = 2$  to gradually increase the feature resolution to  $2^t$ . The other is one-step M2MRF with  $\delta = 2^t$  which directly increases the feature resolution to  $2^t$ . Taking  $t = 2$  for example, Fig.4 illustrates the cascade M2MRF and one-step M2MRF for downsampling and upsampling respectively. Considering the extremely class imbalance in tiny lesion segmentation, Dice loss (Milletari, Navab, and Ahmadi 2016) is adopted to train M2MRF-HRNetV2 for tiny lesion segmentation.

## 4. Experiments and Discussions

To validate the effectiveness of our M2MRF module on tiny lesion segmentation, we carry out experiments on two public datasets i.e. DDR (Li et al. 2019) and IDRiD (Porwal et al. 2020). For evaluation metrics, we follow (Porwal et al. 2020) and utilize Area Under Precision-Recall curve (AUPR). We

also report IoU for its wide application in semantic segmentation.

$S_h, S_w$	$r$	$\alpha$	mAUPR	mIoU
4	4	64	60.93	43.33
<b>8</b>	<b>4</b>	<b>64</b>	<b>61.49</b>	<b>43.80</b>
16	4	64	60.69	42.93
8	2	64	61.13	43.45
<b>8</b>	<b>4</b>	<b>64</b>	<b>61.49</b>	<b>43.80</b>
8	8	64	61.43	43.78
8	4	32	60.34	42.71
<b>8</b>	<b>4</b>	<b>64</b>	<b>61.49</b>	<b>43.80</b>
8	4	128	61.31	43.63

Table 1: M2MRF(cascade/one-step) with different settings on DDR validation set (Li et al. 2019). Results are averaged over three repetitions.

#### 4.1 Implementation Details.

**Datasets and augmentation.** DDR (Li et al. 2019) contains 757 colour fundus images of size ranging from  $1088 \times 1920$  to  $3456 \times 5184$ , among which 383 for training, 149 for validation and 225 for testing. In DDR (Li et al. 2019), 24154, 13035, 1354 and 10563 connected regions are annotated by experts as EXs, HEs, SEs and MAs respectively. To our best knowledge, DDR (Li et al. 2019) is the largest dataset for lesion segmentation in fundus images. IDRiD (Porwal et al. 2020) contains 81 colour fundus images of size  $4288 \times 2848$  among which 54 for training and 27 for testing. It is provided by a grand challenge on “Diabetic Retinopathy – Segmentation and Grading” in 2018. In IDRiD (Porwal et al. 2020), 11716, 1903, 150 and 3505 connected regions are annotated by experts as EXs, HEs, SEs and MAs respectively.

Before feeding images into models, we resize images in DDR (Li et al. 2019) such that the long side is 1024. Those whose short side is less than 1024, zeros are padded. Following (Liu et al. 2021a) and (Guo et al. 2019), images in IDRiD (Porwal et al. 2020) are resized to  $1440 \times 960$ . Three tricks are adopted to augment the training data: multi-scale (0.5-2.0), rotation ( $90^\circ$ ,  $180^\circ$  and  $270^\circ$ ) and flipping(horizontal and vertical).

**Experimental setting.** M2MRF-HRNetV2 is built on the top of implementation of HRNetV2 (Wang et al. 2020) provided by MMSegmentation (Contributors 2020). We initialize parameters associated with both M2MRF and dense classification layers with Gaussian distribution with zeros mean and standard deviation of 0.01 and the rest with the pre-trained model on ImageNet (Krizhevsky, Sutskever, and Hinton 2012). SGD is used for parameters optimisation. Hyper-parameters include: initial learning rate (0.01 poly policy with power of 0.9), weight decay (0.0005), momentum (0.9), batch size (4) and iteration epoch (60k on DDR and 40k on IDRiD).

#### 4.2 Results on DDR and Analysis

**Ablation study for M2MRF.** There are four hyper-parameters in our M2MRF, i.e. the patch size  $S_h$  and  $S_w$ ,

$r$  in channel compressor,  $\alpha$  in Eqn.(6). For  $S_h$  and  $S_w$ , we directly let them equal and conduct experiments with setting  $\{4, 8, 16\}$ . For  $r$  and  $\alpha$ , we conduct experiments with setting  $r$  to  $\{2, 4, 8\}$  and  $\alpha$  to  $\{32, 64, 128\}$  and replacing the strided convolution layer in HRNetV2 (Wang et al. 2020) with our cascade M2MRF and bilinear interpolation layer in HRNetV2 (Wang et al. 2020) with one-step M2MRF. Performance on DDR (Li et al. 2019) validation set is listed in Table 1, from which we can see that  $S_h = S_w = 8$ ,  $r = 4$  and  $\alpha = 64$  yield best performance. In what followed, except for extra illustration,  $S_h = S_w = 8$ ,  $r = 4$  and  $\alpha = 64$  are default setting.

**Comparison to other RF operators.** We verify our proposed M2MRF on DDR (Li et al. 2019) testing set, and compare them with ten pairs of existing RF operators, as listed in Table 2. All the models are build on HRNetV2(Wang et al. 2020) but with different RF operators. The first row is the baseline. For LIP (Gao, Wang, and Wu 2019) and CARAFE (Wang et al. 2019) as downsampling operators, we follow the suggestion by original papers. For CARAFE (Wang et al. 2019) as upsampling operator, the upsample rate is set to be same with scale factor in bilinear interpolation in HRNetV2 (Wang et al. 2020). For CARAFE++ (Wang et al. 2021), same setting to CARAFE is adopted. For IndexNet (Lu et al. 2020) and A<sup>2</sup>U (Dai, Lu, and Shen 2021), they are used to replace the couple of strided convolution in previous stage and bilinear interpolation in subsequent stage. For our M2MRF, we conduct experiments with four different combinations (see Table 2).

Table 2 reports quantitative results. As summarised, among four variants of our M2MRF, M2MRF(one-step/one-step) achieves best. Comparing with vanilla HRNetV2 (Wang et al. 2020), our M2MRF(one-step/one-step) improves the mAUPR by a large margin from 45.21% to 49.94% and the mIoU from 28.84% to 31.16% with few extra parameters (65.85M→69.93M) and slightly slower inference speed (11.31fps→9.21fps). Comparing with existing RF operators, our M2MRF(one-step/one-step) achieves best in both mAUPR and mIoU and the rest three variants achieve better mAUPR and competitive mIoU. Specifically, comparing with the recent learning-based RF operators IndexNet (Lu et al. 2020) and CARAFE++ (Wang et al. 2021), our M2MRF(one-step/one-step) and M2MRF(one-step/cascade) achieve better performance in mAUPR and mIoU with less parameters and competitive FPS. Comparing with A<sup>2</sup>U (Dai, Lu, and Shen 2021), our four variants of M2MRF outperform it on both mAPUR and mIoU with faster inference speed.

**Comparison to state-of-the-art segmentation methods.** We compare our M2MRF-HRNetV2 with nine state-of-the-art segmentation approaches as listed in Table 3. The first seven methods are CNN-based and the rest two are transformer-based. Results by Swin-base (Liu et al. 2021b) are obtained by fine-tuning the ImageNet-22K pre-trained model and the rest are by fine-tuning the ImageNet-1K pre-trained models. As we can see that: (1) comparing with previous CNN-based segmentation methods, the vanilla HRNetV2 (Wang et al. 2020) achieves best performance with both mAUPR 45.21% and mIoU 28.84%; (2) comparing

Downsample	Upsample	mAUPR	mIoU	Param(M)	FPS
StrideConv	Bilinear	45.21	28.84	65.85	11.31
MaxPool	Bilinear	45.97	29.17	<b>59.45</b>	<b>11.88</b>
MaxPool	Unpooling	48.81	<u>30.72</u>	<b>59.45</b>	<u>11.62</u>
LIP(Gao, Wang, and Wu 2019)	Bilinear	43.14	26.29	75.44	6.80
CARAFE(Wang et al. 2019)	Bilinear	46.27	28.51	66.30	9.24
StrideConv	CARAFE	46.68	29.97	72.12	10.26
StrideConv	Deconv	46.24	29.37	73.12	10.86
IndexNet(Lu et al. 2020)	IndexNet	48.06	30.28	70.33	10.75
CARAFE++(Wang et al. 2021)	CARAFE++	47.64	29.54	72.57	8.69
A <sup>2</sup> U(Dai, Lu, and Shen 2021)	A <sup>2</sup> U	45.89	29.27	66.51	3.97
M2MRF(one-step)	M2MRF(one-step)	<b>49.94</b>	<b>31.16</b>	69.93	9.21
M2MRF(one-step)	M2MRF(cascade)	<u>49.42</u>	30.41	67.15	8.54
M2MRF(cascade)	M2MRF(one-step)	48.94	30.09	70.30	8.49
M2MRF(cascade)	M2MRF(cascade)	49.25	30.27	67.52	8.01

Table 2: Comparing with different RF operators on DDR (Li et al. 2019) testing set. The first row is the baseline i.e. vanilla HRNetV2 (Wang et al. 2020). The Best and Second Best results are highlighted in boldface and underlined respectively. Results are averaged over three repetitions.

Method	AUPR					IoU				
	EX	HE	SE	MA	mAUPR	EX	HE	SE	MA	mIoU
HED(Xie and Tu 2015)	61.40	43.19	46.68	20.61	42.97	39.50	27.09	29.46	12.63	27.17
DNL(Yin et al. 2020)	56.05	47.81	42.01	14.71	40.14	36.39	27.15	25.33	8.46	24.33
Deeplabv3+(Chen et al. 2018)	62.32	40.79	41.83	24.39	42.34	41.44	23.44	26.46	14.55	26.47
PSPNet(Zhao et al. 2017)	59.93	43.93	43.51	19.90	41.82	39.11	25.89	27.08	11.88	25.99
SPNet(Hou et al. 2020)	57.04	42.71	42.32	14.85	39.23	37.31	24.51	26.64	8.75	24.31
L-seg (Guo et al. 2019)	55.46	35.86	26.48	10.52	32.08	-	-	-	-	-
HRNetV2(Wang et al. 2020)	61.55	45.68	46.91	26.70	45.21	41.82	29.01	28.94	15.60	28.84
Swin-base(Liu et al. 2021b)	62.75	<b>57.56</b>	48.52	23.31	48.03	42.71	<b>37.01</b>	32.30	13.16	<b>31.29</b>
Twins-SVT-B (Chu et al. 2021)	59.71	49.96	<u>52.72</u>	22.03	46.11	39.70	29.08	<b>36.24</b>	12.07	29.28
M2MRF(one-step/one-step)-HRNetV2	<b>64.17</b>	54.20	<b>53.19</b>	28.21	<b>49.94</b>	43.35	30.03	<u>35.22</u>	16.06	<u>31.16</u>
M2MRF(one-step/cascade)-HRNetV2	63.88	<u>55.47</u>	50.01	28.33	<u>49.42</u>	43.06	<u>30.56</u>	32.08	15.95	30.41
M2MRF(cascade/one-step)-HRNetV2	63.59	54.43	49.35	<u>28.38</u>	<u>48.94</u>	<u>43.49</u>	29.17	31.39	<b>16.31</b>	30.09
M2MRF(cascade/cascade)-HRNetV2	<b>64.17</b>	54.72	49.64	<b>28.46</b>	49.25	<b>44.04</b>	29.28	31.60	<u>16.15</u>	30.27

Table 3: Segmentation results on DDR test set (Li et al. 2019). The results are averaged over three repetitions.

with vanilla HRNetV2 (Wang et al. 2020), the four variants of our M2MRF get better performance on the four lesion classes consistently in terms of both mAUPR and mIoU; (3) comparing with transformer-based methods, i.e., Swin-base (Liu et al. 2021b) and Twins-SVT-B (Chu et al. 2021), our four variants of M2MRF achieve better on mAUPR. Fig. 5 shows more visualisation results of our M2MRF-HRNetV2 and the vanilla HRNetV2 (Wang et al. 2020) on DDR test set (Li et al. 2019). In the first example, we can see that our M2MRF(one-step/one-step)-HRNetV2 is able to segment out the two SEs (delineated in yellow) even though they are surrounded by HEs (delineated in green). On the contrary, the vanilla HRNetV2 (Wang et al. 2020) fails to well segment them out. In clinical, HEs and MAs belong to red lesions. The difference between small HEs and MAs is subtle. Thus our method wrongly classifies the small HEs as MAs. However, more worse, those small HEs are directly ignored by vanilla HRNetV2 and wrongly classified as background. In the second and third examples, tiny EXs

pointed out by white arrows are correctly segmented out by our method while miss-classified by vanilla HRNetV2.

### 4.3 Results on IDRiD

#### Comparison to state-of-the-art segmentation methods.

We compare our M2MRF with four tiny lesion segmentation methods (VRT, PATech, iFLYTEK (Porwal et al. 2020) and L-seg (Guo et al. 2019)), six state-of-the-art CNN-based methods and two transformer-based methods(Swin-base (Liu et al. 2021b) and Twins-SVT-B (Chu et al. 2021)) as listed in Table 4. Performance of semantic segmentation approaches is obtained via fine-tuning on IDRiD (Porwal et al. 2020) training set. Among four tiny lesion segmentation methods, performance of L-Seg (Guo et al. 2019) is directly borrowed from original paper and the rest are top three methods borrowed from the 2018 ISBI grand challenge. From Table 4, we have following observations: (1) methods specially designed for lesion segmentation achieve better mAUPR than the compared CNN-based methods except

Method	AUPR					IoU				
	EX	HE	SE	MA	mAUPR	EX	HE	SE	MA	mIoU
VRT(1st)(Porwal et al. 2020)	71.27	<u>68.04</u>	<b>69.95</b>	<u>49.51</u>	64.69	-	-	-	-	-
PATech(2nd)(Porwal et al. 2020)	<b>88.50</b>	64.90	-	47.70	-	-	-	-	-	-
iFLYTEK(3rd)(Porwal et al. 2020)	87.41	55.88	65.88	<b>50.17</b>	64.84	-	-	-	-	-
L-seg(Guo et al. 2019)	79.45	63.74	71.13	46.27	65.15	-	-	-	-	-
HED(Xie and Tu 2015)	80.81	66.41	68.09	40.45	63.94	64.74	47.43	50.38	24.07	46.66
DNL(Yin et al. 2020)	75.12	64.04	64.73	32.48	59.09	57.67	44.80	47.03	19.61	42.28
Deeplabv3+(Chen et al. 2018)	81.93	64.66	63.04	43.14	63.19	66.10	44.90	44.39	25.45	45.21
PSPNet(Zhao et al. 2017)	75.21	63.36	63.65	32.71	58.73	57.78	43.71	45.81	19.50	41.70
SPNet(Hou et al. 2020)	64.61	54.11	52.14	30.14	50.25	44.40	28.50	33.58	14.72	30.30
HRNetV2(Wang et al. 2020)	82.09	65.50	68.68	43.76	65.01	<u>66.57</u>	45.56	50.99	26.98	47.52
Swin-base(Liu et al. 2021b)	81.30	67.70	66.46	44.19	64.91	66.17	<b>49.72</b>	49.27	28.28	48.36
Twins-SVT-B (Chu et al. 2021)	80.09	63.12	68.86	43.27	63.84	64.68	44.91	<b>51.76</b>	26.92	47.07
M2MRF(one-step/one-step)-HRNetV2	82.04	67.80	68.23	47.86	66.48	66.16	48.87	50.03	31.23	49.07
M2MRF(one-step/cascade)-HRNetV2	81.98	67.41	66.68	47.91	66.00	66.07	48.58	48.16	31.42	48.56
M2MRF(cascade/one-step)-HRNetV2	82.16	<b>68.69</b>	<u>69.32</u>	48.80	<b>67.24</b>	66.46	<b>49.72</b>	<u>51.43</u>	<b>32.13</b>	<b>49.94</b>
M2MRF(cascade/cascade)-HRNetV2	82.29	66.94	<u>69.00</u>	48.43	<u>66.66</u>	<b>66.62</b>	48.04	50.98	<u>31.81</u>	<u>49.36</u>

Table 4: Results on IDRiD (Porwal et al. 2020). Results are averaged over three repetitions.

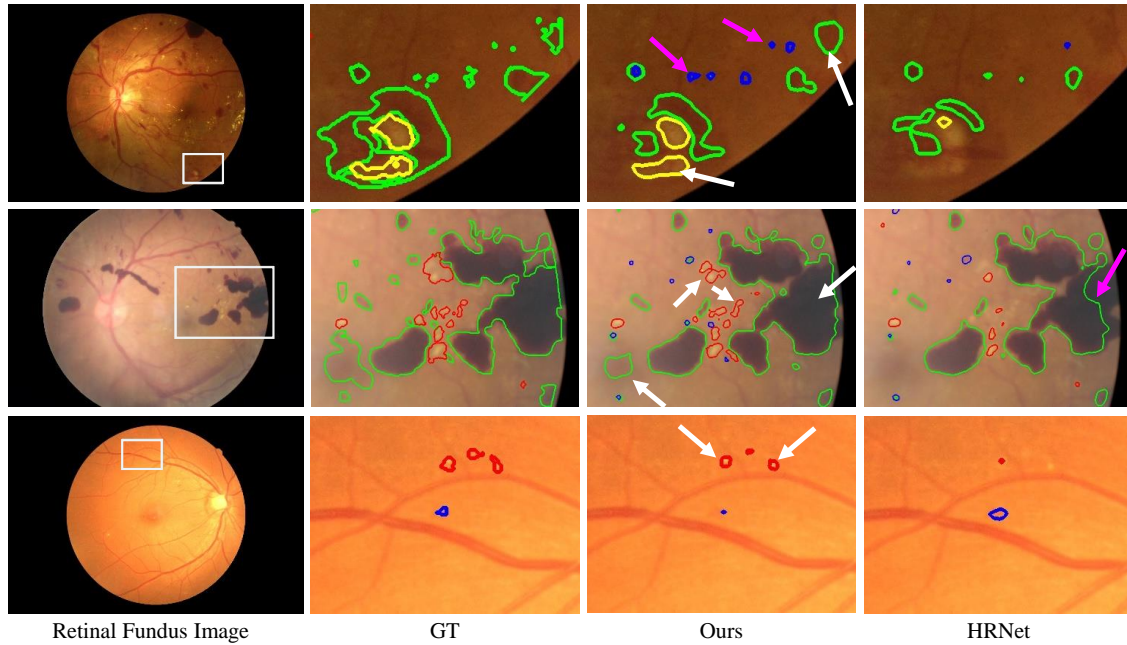


Figure 5: Visualization results on DDR. From left to right are retinal fundus images, image patches with GT annotations, segmentation results by our M2MRF(one-step/one-step)-HRNetV2, results by vanilla HRNetV2. Regions delineated in green, blue, red and yellow are HEs, MAs, EXs and SEs by experts or segmentation approaches. White arrows point out example lesions that are correctly segmented out by ours while wrongly classified by vanilla HRNetV2. Magenta arrows point out lesions that wrongly classified by segmentation approaches.

for HRNetV2 (Wang et al. 2020); (2) HRNetV2 (Wang et al. 2020) achieves competitive mAUPR to methods participating grand challenge as it learns high-resolution representations which contains spatial information; (3) Equipped with our four variants of M2MRF, HRNetV2 is able to achieve better performance than all of the compared CNN-based

methods and the two transformer-based methods; (4) The four variants of M2MRF contribute significantly to MA segmentation and outperforms the plain HRNetV2 (Wang et al. 2020) by more than 4% on AUPR and 4% on IoU, which indicates that our M2MRF is able to maintain more tiny structure information. Fig.6 shows the segmentation results by

Downsample	Upsample	mAUPR	mIoU
StrideConv	Bilinear	65.01	47.52
MaxPool	Bilinear	66.24	49.28
CARAFE	Bilinear	66.27	48.93
LIP	Bilinear	63.04	45.78
StrideConv	Deconv	64.64	47.23
MaxPool	Unpooling	66.17	49.22
StrideConv	CARAFE	63.63	45.77
CARAFE++	CARAFE++	65.64	48.23
IndexNet	IndexNet	64.66	47.36
A <sup>2</sup> U	A <sup>2</sup> U	64.65	47.32
M2MRF(one-step)	M2MRF(one-step)	66.48	49.07
M2MRF(one-step)	M2MRF(cascade)	66.00	48.56
M2MRF(cascade)	M2MRF(one-step)	<b>67.24</b>	<b>49.94</b>
M2MRF(cascade)	M2MRF(cascade)	66.66	49.36

Table 5: Comparing with different RF operators on IDRiD (Porwal et al. 2020) testing set. The first row is the baseline i.e. vanilla HRNetV2 (Wang et al. 2020). Results are averaged over three repetitions.

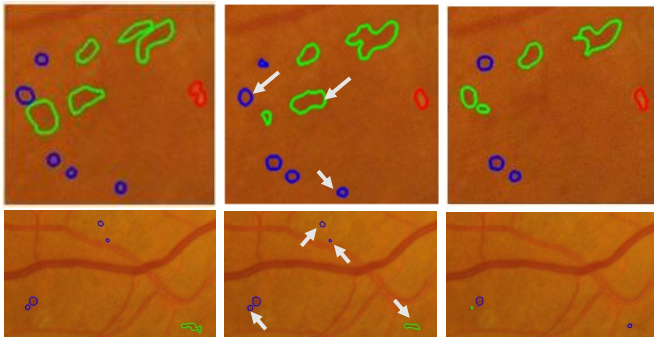


Figure 6: Segmentation results on IDRiD. Left: patches with lesion annotations by experts; Middle: results by our M2MRF(one-step/cascade)-HRNetV2; Right: results by vanilla HRNetV2 (Wang et al. 2020). Regions delineated in green, blue and red are HEs, MAs and EXs by experts or segmentation approaches. Lesions that are correctly segmented out by ours while missed by vanilla HRNetV2 (Wang et al. 2020) are pointed out by white arrows.

M2MRF(cascade/one-step)-HRNetV2 and the vanilla HRNetV2 (Wang et al. 2020). More results will be provided in supplementary.

**Comparison to state-of-the-art RF operators.** Table 5 reports the results of our four variants of M2MRF and state-of-the-art RF operators on IDRiD (Porwal et al. 2020). It shows that the cascade M2MRF for downsampling and one-step M2MRF as upsampling achieves best performance. Interestingly, two pairs of rule-based RF operators, i.e., MaxPool/bilinear and MaxPool/unpooling achieve better than previous learning-based RF operators. The possible reason is that it may be difficult for learning-based RF operators to preserve activations caused by tiny lesions via learning from a small local region with limited size of receptive field.

## Conclusion

We present a simple RF operator named M2MRF for feature reassembly which unifies feature downsampling and upsampling in one framework. Our M2MRF considers contributions of long range spatial dependencies and simultaneously reassembles multiple features in a large region to multiple target features once. Thus, it is able to maintain activations caused by tiny lesions during feature reassembly. It shows significant improvements on two public tiny lesion segmentation datasets, i.e. DDR (Li et al. 2019) and IDRiD (Porwal et al. 2020). Moreover, our M2MRF only introduces marginal extra parameters and could be used to replace arbitrary RF operators in existing CNN architectures.

## References

- Badrinarayanan, V.; Kendall, A.; and Cipolla, R. 2017. Segnet: A deep convolutional encoder-decoder architecture for image segmentation. *TPAMI*, 39(12): 2481–2495.
- Chen, L.-C.; Papandreou, G.; Kokkinos, I.; Murphy, K.; and Yuille, A. L. 2017. Deeplab: Semantic image segmentation with deep convolutional nets, atrous convolution, and fully connected crfs. *TPAMI*, 40(4): 834–848.
- Chen, L.-C.; Zhu, Y.; Papandreou, G.; Schroff, F.; and Adam, H. 2018. Encoder-decoder with atrous separable convolution for semantic image segmentation. In *ECCV*, 801–818.
- Chen, W.; Zhu, X.; Sun, R.; He, J.; Li, R.; Shen, X.; and Yu, B. 2020. Tensor Low-Rank Reconstruction for Semantic Segmentation. In *ECCV*, 52–69. Springer.
- Choi, S.; Kim, J. T.; and Choo, J. 2020. Cars Can’t Fly Up in the Sky: Improving Urban-Scene Segmentation via Height-Driven Attention Networks. In *CVPR*, 9373–9383.
- Chu, X.; Tian, Z.; Wang, Y.; Zhang, B.; Ren, H.; Wei, X.; Xia, H.; and Shen, C. 2021. Twins: Revisiting the Design of Spatial Attention in Vision Transformers. arXiv:2104.13840.
- Contributors, M. 2020. MMSegmentation: OpenMMLab Semantic Segmentation Toolbox and Benchmark. <https://github.com/open-mmlab/mms Segmentation>.
- Cordts, M.; Omran, M.; Ramos, S.; Rehfeld, T.; Enzweiler, M.; Benenson, R.; Franke, U.; Roth, S.; and Schiele, B. 2016. The cityscapes dataset for semantic urban scene understanding. In *CVPR*, 3213–3223.
- Dai, J.; Qi, H.; Xiong, Y.; Li, Y.; Zhang, G.; Hu, H.; and Wei, Y. 2017. Deformable convolutional networks. In *ICCV*, 764–773.
- Dai, Y.; Lu, H.; and Shen, C. 2021. Learning Affinity-Aware Upsampling for Deep Image Matting. In *CVPR*, 6841–6850.
- Decenciere, E.; Cazuguel, G.; Zhang, X.; Thibault, G.; Klein, J.-C.; Meyer, F.; Marcotegui, B.; Quéllec, G.; Lamard, M.; Danno, R.; et al. 2013. TeleOphta: Machine learning and image processing methods for teleophthalmology. *Irbm*, 34(2): 196–203.
- Dong, X.; Bao, J.; Chen, D.; Zhang, W.; Yu, N.; Yuan, L.; Chen, D.; and Guo, B. 2021. CSWin Transformer: A General Vision Transformer Backbone with Cross-Shaped Windows. arXiv:2107.00652.

- Du, J.; Zou, B.; Chen, C.; Xu, Z.; and Liu, Q. 2020. Automatic microaneurysm detection in fundus image based on local cross-section transformation and multi-feature fusion. *Computer Methods and Programs in Biomedicine*, 196: 105687.
- Fu, J.; Liu, J.; Jiang, J.; Li, Y.; Bao, Y.; and Lu, H. 2020. Scene segmentation with dual relation-aware attention network. *TNNLS*.
- Fu, J.; Liu, J.; Tian, H.; Li, Y.; Bao, Y.; Fang, Z.; and Lu, H. 2019. Dual attention network for scene segmentation. In *CVPR*, 3146–3154.
- Gao, Z.; Wang, L.; and Wu, G. 2019. Lip: Local importance-based pooling. In *ICCV*, 3355–3364.
- Guo, S.; Li, T.; Kang, H.; Li, N.; Zhang, Y.; and Wang, K. 2019. L-Seg: An end-to-end unified framework for multi-lesion segmentation of fundus images. *Neurocomputing*, 349: 52–63.
- Hou, Q.; Zhang, L.; Cheng, M.-M.; and Feng, J. 2020. Strip pooling: Rethinking spatial pooling for scene parsing. In *CVPR*, 4003–4012.
- Huang, Z.; Wang, X.; Huang, L.; Huang, C.; Wei, Y.; and Liu, W. 2019. Cnet: Criss-cross attention for semantic segmentation. In *ICCV*, 603–612.
- Krizhevsky, A.; Sutskever, I.; and Hinton, G. E. 2012. ImageNet classification with deep convolutional neural networks. In *NeurIPS*, 84–90. AcM New York, NY, USA.
- LeCun, Y.; Boser, B. E.; Denker, J. S.; Henderson, D.; Howard, R. E.; Hubbard, W. E.; and Jackel, L. D. 1990. Handwritten digit recognition with a back-propagation network. In *NeurIPS*, 396–404.
- Li, T.; Gao, Y.; Wang, K.; Guo, S.; Liu, H.; and Kang, H. 2019. Diagnostic assessment of deep learning algorithms for diabetic retinopathy screening. *Information Sciences*, 501: 511–522.
- Li, X.; Zhao, H.; Han, L.; Tong, Y.; Tan, S.; and Yang, K. 2020. Gated Fully Fusion for Semantic Segmentation. In *AAAI*, volume 34, 11418–11425.
- Liu, Q.; Liu, H.; Zhao, Y.; and Liang, Y. 2021a. Dual-Branch Network with Dual-Sampling Modulated Dice Loss for Hard Exudate Segmentation in Colour Fundus Images. *IEEE Journal of Biomedical and Health Informatics*, 1–1.
- Liu, Q.; Zou, B.; Chen, J.; Ke, W.; Yue, K.; Chen, Z.; and Zhao, G. 2017. A location-to-segmentation strategy for automatic exudate segmentation in colour retinal fundus images. *Computerized medical imaging and graphics*, 55: 78–86.
- Liu, Z.; Lin, Y.; Cao, Y.; Hu, H.; Wei, Y.; Zhang, Z.; Lin, S.; and Guo, B. 2021b. Swin transformer: Hierarchical vision transformer using shifted windows. In *ICCV*.
- Long, J.; Shelhamer, E.; and Darrell, T. 2015. Fully convolutional networks for semantic segmentation. In *CVPR*, 3431–3440.
- Lu, H.; Dai, Y.; Shen, C.; and Xu, S. 2019. Indices matter: Learning to index for deep image matting. In *ICCV*, 3266–3275.
- Lu, H.; Dai, Y.; Shen, C.; and Xu, S. 2020. Index networks. *TPAMI*.
- Milletari, F.; Navab, N.; and Ahmadi, S. 2016. V-Net: Fully Convolutional Neural Networks for Volumetric Medical Image Segmentation. In *2016 Fourth International Conference on 3D Vision (3DV)*, 565–571.
- Noh, H.; Hong, S.; and Han, B. 2015. Learning deconvolution network for semantic segmentation. In *ICCV*, 1520–1528.
- Porwal, P.; Pachade, S.; Kokare, M.; Deshmukh, G.; Son, J.; Bae, W.; Liu, L.; Wang, J.; Liu, X.; Gao, L.; et al. 2020. IDRiD: Diabetic Retinopathy–Segmentation and Grading Challenge. *Medical Image Analysis*, 59: 101561.
- Ronneberger, O.; Fischer, P.; and Brox, T. 2015. U-net: Convolutional networks for biomedical image segmentation. In *MICCAI*, 234–241. Springer.
- Springenberg, J. T.; Dosovitskiy, A.; Brox, T.; and Riedmiller, M. 2015. Striving for simplicity: The all convolutional net. In *ICLR workshop*.
- Sun, K.; Xiao, B.; Liu, D.; and Wang, J. 2019. Deep high-resolution representation learning for human pose estimation. In *CVPR*, 5693–5703.
- Wang, J.; Chen, K.; Xu, R.; Liu, Z.; Loy, C. C.; and Lin, D. 2019. Carafe: Content-aware reassembly of features. In *ICCV*, 3007–3016.
- Wang, J.; Chen, K.; Xu, R.; Liu, Z.; Loy, C. C.; and Lin, D. 2021. CARAFE++: Unified Content-Aware ReAssembly of FEatures. *IEEE Transactions on Pattern Analysis and Machine Intelligence*.
- Wang, J.; Sun, K.; Cheng, T.; Jiang, B.; Deng, C.; Zhao, Y.; Liu, D.; Mu, Y.; Tan, M.; Wang, X.; et al. 2020. Deep high-resolution representation learning for visual recognition. *TPAMI*.
- Xie, S.; and Tu, Z. 2015. Holistically-nested edge detection. In *ICCV*, 1395–1403.
- Yin, M.; Yao, Z.; Cao, Y.; Li, X.; Zhang, Z.; Lin, S.; and Hu, H. 2020. Disentangled non-local neural networks. In *ECCV*, 191–207. Springer.
- Zeiler, M. D.; and Fergus, R. 2014. Visualizing and understanding convolutional networks. In *ECCV*, 818–833. Springer.
- Zeiler, M. D.; Taylor, G. W.; and Fergus, R. 2011. Adaptive deconvolutional networks for mid and high level feature learning. In *ICCV*, 2018–2025. IEEE.
- Zhang, X.; Thibault, G.; Decencière, E.; Marcotegui, B.; Laÿ, B.; Danno, R.; Cazuguel, G.; Quellec, G.; Lamard, M.; Massin, P.; et al. 2014. Exudate detection in color retinal images for mass screening of diabetic retinopathy. *Medical image analysis*, 18(7): 1026–1043.
- Zhao, H.; Shi, J.; Qi, X.; Wang, X.; and Jia, J. 2017. Pyramid scene parsing network. In *CVPR*, 2881–2890.